Magnetization Compensation Temperature and Frustration-Induced Topological Defects in Ferrimagnetic Antiperovskite math xmlns="http://www.w3.org/1998/Math/MathML" display="inline">mrow>msub>mrow>mi>Mn/mi>/mrow> mrow>mn>4/mn>/mrow>/msub>mi mathvariant="normal">N/mi>/mrow>/math>

Temuujin Bayaraa, Changsong Xu, and L. Bellaiche

Phys. Rev. Lett. **127**, 217204 — Published 18 November 2021

DOI: 10.1103/PhysRevLett.127.217204

Magnetization compensation temperature and frustration-induced topological defects in ferrimagnetic anti-perovskite Mn_4N

Temuujin Bayaraa[1], Changsong Xu[1,2*], and L. Bellaiche[1,2]

[1]Physics Department, University of Arkansas, Fayetteville, Arkansas 72701, United States
[2]Institute for Nanoscience and Engineering, University of Arkansas, Fayetteville, Arkansas 72701, United States

Abstract

First-principles-based simulations are conducted to investigate magnetic properties and topological spin textures in the anti-perovskite Mn_4N ferrimagnet. A magnetization compensation temperature, resulting from a competition between different Mn sublattices, is found in this system, when under thermal equilibrium. Striking metastable topological states are also discovered, including nanometric hedgehog-anti-hedgehog pairs that originate from frustrated exchange interactions rather than the usual Dzyaloshinskii-Moriya interaction.

Antiperovskites have the same crystallographic structure as perovskites, but with cations and anions having inverted positions. For instance, in the prototypical $BaTiO_3$ perovskite, the O anions are three times more numerous than the Ba or Ti cations, while in the Sr_3SnO antiperovskite [1], Sr cations are thrice more present than O anions (or Sn cations). Antiperovskites can display promising properties such as superconductivity [2] and topological band gaps [3–5]. In particular, Mn_4N is a ferrimagnetic antiperovskite, because Mn cations at different sites have unequal magnetic moments (it can be viewed as having the Mn_3MnN stoichiometry with Mn ions on different sublattices). It is receiving growing attention, due to its perpendicular magnetic anisotropy (PMA) and ultrafast response to external field [6–15].

Ferrimagnets can have many promising features, such as a so-called magnetization compensation temperature at which the total magnetization (M_S) vanishes, as a result of cancellation between magnetic moments of different sublattices. Compensation temperatures have been found in, e.g., rare-earth iron garnets [16–19], rare-earth orthoferrites and orthochromates [20,21], and amorphous rare-earth transition-metal compounds [22–25]. One importance of such compensation temperature is to give rise to the antiferromagnetic-like dynamics in ferrimagnets and lead to high-speed domain walls motion [22,26]. Magnetization switching is easily achieved with faster domain walls which makes such materials a promising candidate for high-density data storage. Furthermore, ferrimagnets with small M_S and PMA allow them to host ultrasmall and fast skyrmions at room temperature [22–24], which is promising for achieving high-density, low-cost, and energy-efficient skyrmionic device technology.

In contrast, we are not aware that magnetization compensation temperature and magnetic topological defects have been reported in any antiperovskite ferrimagnet. Finding them in, e.g., Mn_4N will open a new door to designing spintronic devices. One may also wonder what are their driving mechanisms. Are these hypothetical topological defects generated by a mechanism that differs from the dipole-dipole interactions [27] or Dzyaloshinskii-Moriya interactions [28]? If yes, finding such a mechanism will deepen the understanding of topologies and magnetism.

The goal of this Letter is to provide an answer to all these open questions by performing first-principles calculations and *ab-initio* based Monte Carlo simulations. We reveal the existence of a sizeable magnetization compensation temperature that is driven by the different temperature behavior of three types of magnetic Mn ions when Mn_4N is in thermal equilibrium. We also report the discovery of metastable topological states, including nanometric hedgehog-anti-hedgehog pairs (HAPs), that are induced by frustrated exchange interactions.

Here, we used first-principle-based approaches to study the magnetic properties of Mn_4N. As revealed by the neutron diffraction experiment of Ref. [15], two types of magnetic configurations can exist in Mn_4N. The one shown in Fig. 1a is denoted as the Type-B structure. It possesses spins of Mn I and Mn II that are parallel to each other while being antiparallel to the spins of Mn III (A,B). The second one has been coined Type-A and exhibits spins of Mn II and Mn III that are parallel to each other and antiparallel to those of Mn I. Our first-principles calculations

conducted at 0K predict that the Type-B structure has lower energy than Type-A – as consistent with Refs [7,15].

We construct the following spin Hamiltonian for Mn_4N:

$$H = H^{DEC} + H^{DMI} + H^{SIA}, \quad (1)$$

with

$$H^{DEC} = \sum_{<i,j>^A}^{1NN-4NN} \sum_{\alpha}^{x,y,z} J^A_{\alpha\alpha} S_i^\alpha S_j^\alpha$$

$$H^{DMI} = \sum_{<i,j>} \boldsymbol{D} \cdot \boldsymbol{S}_i \times \boldsymbol{S}_j$$

$$H^{SIA} = \sum_i \boldsymbol{S}_i \cdot \boldsymbol{A}_{ii} \cdot \boldsymbol{S}_i, \quad (2)$$

where H^{DEC}, H^{DMI}, H^{SIA} represent energies from the diagonal exchange coupling, Dzyaloshinskii-Moriya interaction (DMI) [29], and single-ion anisotropy (SIA) [30], respectively. The sum over <i,j> and NN denote the different magnetic pairs and maximum nearest-neighbor interactions that are considered here, respectively. The sum over i runs through all magnetic sites. Spins (S) are set to be 1 and their values are absorbed by the magnetic exchange coupling (J) parameters.

All considered magnetic parameters are determined from density functional theory (DFT, see Supplemental Material) and are shown in Tables 1 and 2, while the schematics of the magnetic exchange interactions are shown in Fig. 1(b). To accurately predict magnetic properties, it is necessary to include interactions up to the 4th nearest neighbors (such interactions are denoted as J_{41}, J_{42}), which corresponds to a distance of 4.755Å. Note that 5th and 6th nearest-neighbor interactions have been considered as shown in Supplemental Material. The last column of Table 1 reports the energy contribution of each J coupling parameter of the total energy of the Type-B ferrimagnetic ground state with respect to the paramagnetic state, as resulting from the use of the Hamiltonian of Eqs. (1) and (2).

Table I shows that the J_{11}'s are positive and thus favor an antiparallel arrangement between the first-nearest neighbor (1NN) Mn II and Mn III(B) ions, as consistent with the ferrimagnetic Type-B structure. Similarly, the J_{12}'s adopt positive values, which are in-line with the antiparallel alignment between 1NN Mn I and Mn III(A) spins within Type-B. The J_{14}'s are negative and therefore push the 1NN MnI and MnII ions to adopt a parallel alignment, which once again favors Type-B. On the other hand, the J_{13}'s coupling parameters are positive and therefore would prefer to have spins of 1NN Mn III(A) and Mn III(B) ions to be antiparallel to each other. This tendency contrasts with the arrangement of such spins within Type-B, which explains why it induces a positive (unfavorable) change in energy with respect to the paramagnetic structure. The J_{13} coupling parameters, and any other exchange parameters that lead to an increase in energy of the Type-B structure (with respect to the paramagnetic state), will be called here frustrated

exchange parameters [31]. We found that the parallel alignment between Mn III(A) and Mn III(B) ions within Type-B mainly originates from the strong positive J_{11} and J_{12} (indirect) interactions.

Moreover, second nearest neighbor (2NN) exchange coupling parameters between in-plane Mn I - Mn I pairs (J_{21}), in-plane Mn III(A) - Mn III(A) pairs (J_{22}), in-plane Mn III(B) - Mn III(B) pairs (J_{23}), out-of-plane Mn I - Mn I pairs (J_{24}), and out-of-plane Mn II - Mn II pairs (J_{25}), are all negative and thus favor ferromagnetic (FM) interactions between these pairs, as consistent with Type-B (*cf* Fig 1(b)). On the other hand, the exchange coupling parameters between out-of-plane Mn III(B) - Mn III(B) pairs (J_{26}) and in-plane Mn (II) - Mn (II) pair (J_{27}) are positive and lead to a raise in energy with respect to the paramagnetic state. J_{26} and J_{27} are thus also frustrated exchange parameters. The strongest-in-magnitude magnetic exchange coupling interaction in the Mn_4N system is the 2NN interaction between in-plane Mn I - Mn I pairs, namely the J_{21} term that has a -90.1 meV value. Table 1 also reveals that the 3rd nearest neighbor (3NN) and the 4th nearest neighbor (4NN) magnetic exchange coupling parameters are weaker than the exchange coupling parameters of 1NN and 2NN. In particular, 3NN J parameters between Mn II - Mn I pairs (J_{31}) and Mn III(A) - Mn III(B) pair (J_{32}) are negative and the 4NN parameter between Mn I - Mn III(A) pairs (J_{42}) is positive, with all these three J_{31}, $J_{32,}$ and J_{42} coefficients, therefore favoring Type-B. On the other hand, the exchange parameter between Mn II – Mn III(B) 4NN pairs (J_{41}) is a frustrated exchange parameter.

The extracted DMI vectors for 1NN interactions are almost negligible (as consistent with the fact that 1NN spins are aligned almost parallel to each other and there is no heavy element to induce strong spin-orbit coupling), as indicated by Table 2, and the magnitude of the DMI vectors is about three orders of magnitude smaller than the 1NN J parameters. Table 2 also shows the SIA parameters for all types of Mn ions. The SIA of Mn II is the strongest one and is two orders of magnitude smaller than the strongest J value while being of the same order as the strongest DMI parameter.

Monte Carlo (MC) simulations [32] with a conjugate gradient (CG) method [33] are performed using the DFT extracted magnetic parameters of Tables 1 and 2 and the Hamiltonian of Eqs. (1) and (2), to predict magnetic properties of Mn_4N (see Supplemental Material). Figure 2a shows the specific heat while Figure 2b reports the total normalized magnetization, both as a function of temperature. The specific heat exhibits one peak at a Curie temperature T_C of around 700K, which is in good agreement with the experimental value of 745K [6], which testifies the accuracy of our calculations. Figure 2b also shows that, at T_C, each magnetic sublattice begins to be spontaneously magnetized toward positive values for the Mn I and Mn II atoms but negative ones for the Mn III atoms, as consistent with Type-B. Below T_C and down to about 500K, the magnetizations from the Mn I and Mn II sublattices dominate, making the total magnetization positive. However, the magnitude of the magnetization of the Mn II sublattice increases much smaller than that of the Mn I and, especially, Mn III sublattices as the temperature lowers. As shown in Fig. 2(b), the total magnetization changes its sign at a compensation temperature, T_M, of around 496K. We are not aware of any findings of T_M in this system. However, there is a recent observation of a sign-flip of the anomalous Hall resistance between 498K and 573K [34]

in Mn_4N thin films on GaN, which may be consistent with our predicted T_M. Note also that a magnetization compensation temperature was measured in Mn_4N doped with Co and Ni [35,36], and was also determined to be alterable by epitaxial strain [19] (see Supplemental Material for details).

In addition to the ferrimagnetic Type-B ground state, metastable states, consisting of HAPs [37], were identified from MC calculation results (HAPs were, e.g., observed in MnGe [37] and $MnSi_{1-x}Ge_x$ [38] compounds, but never in antiperovskites). The spin texture and distribution of topological charge, Q, of HAPs are shown in Fig. 3 for a small temperature, using the definition of Berg and Lüstcher [39] for discrete lattice spins [40]. The hedge and anti-hedgehog each have a ~ $8\text{Å} \times 8\text{Å}$ area in the (x,y) plane, and the distance between the bottom of one defect to the top of the other defect forming the pair is ~10Å along the c-axis. Figure 3b shows a hedgehog-anti-hedgehog lattice, with the overall distance between the core of the hedgehog in one pair and the core of the anti-hedgehog in the nearest pairs (illustrated by the black arrows in Fig. 3b) being 18Å. Such nanometric topological defects are appealing for nanoelectronics (cubic-lattice skyrmion was observed to be ~3nm in MnGe [37]) and could lead to novel functionality and devices [41]. We are not aware of any previous finding of topological states in Mn_4N. The spins of the hedgehog and anti-hedgehog predicted here have components parallel to the surface, in addition to the whirling of spins around its core, which is reminiscent of the hedgehog and anti-hedgehogs found in MnGe [37] and $MnSi_{1-x}Ge_x$ [38]. Note that the energy differences between topological spin textures shown in Fig. 3(a) and (b), respectively, and the ferrimagnetic Type-B ground state are rather small, namely about 3 meV/Mn. and 0.5 meV/Mn, respectively. It is thus likely that these topological states can be observed by applying a magnetic field, as similar to the three-dimensional chiral magnetic texture called the hedgehog lattice seen under external magnetic field in MnGe compound [37,38].

Let us find out the microscopic origin behind these topological states. We thus calculate the relative decomposed energy contributions of each J parameter toward the formation of HAPs shown in Fig. 3a with respect to the ferrimagnetic ground state, as displayed in Fig. 4. Two exchange frustrated J parameters, namely J_{26} and J_{41}, have a negative decomposed energy (negative energies represent the tendency toward the metastable HAPs' phase). We also ran MC calculations followed by the CG method from the metastable state shown in Fig. 3a, but with the flipping of the signs of the frustrated J_{26} and J_{41}, to nullify the magnetic exchange frustration in the system (*i.e.*, such change in sign does not make them frustrated anymore). We find that the HAPs then disappear and only the ferrimagnetic ground state is found. We also find that J_{41} is the main contributor to the formation of HAPs pairs, as consistent with Fig. 4 revealing that J_{41} has about 4 times lower decomposed energy contribution with respect to J_{26}.

Furthermore, the decomposed energies of SIA of Mn II and Mn III have negative values (see Figs. 4(f)) and thus favor the formation of the topological state too. The decomposed energy of SIA of Mn II is calculated to not only be the strongest but also to contribute to the formation of HAPs on a scale that is comparable to that of J_{26}. However, switching off these SIA coefficients in the MC simulations does *not* make the HAPs disappear, thus indicating that they are much less important than J_{41} to create and stabilize these topological pairs.

Figure 4(e) also reports the decomposed energy contributions of the DMI vectors. The DMI vector (D_{13}), corresponding to an interaction between the 1NN Mn III(A) and Mn III(B) ions, with these two types of ions also sharing the frustrated J_{13} parameter, has negative energy and thus further contributes to the stabilization of the topological state. However, this contribution is rather weak since the decomposed energy of D_{13} is about three orders smaller than the decomposed energies of J_{26} and J_{41} interactions. In fact, we numerically checked the effect of DMI vectors on the formation of the HAPs by not considering them in our MC simulations and did not find any noticeable change from it: these pairs remain even when all DMI coefficients are switched off, therefore demonstrating that DMI is not the main contributor for these topological pairs. This result is remarkable since DMI is typically the microscopic reason behind the stabilization of (non-collinear) topological states such as skyrmion [42], anti-skyrmion [43], and bimerons [44–46]. Our numerical experiments indicated above, along with Fig. 4, reveal that it is the frustrated J_{41} parameter (and to some lesser extent the frustrated J_{26} coefficient too) that stabilizes such pairs in Mn_4N. Our present finding allows to connect antiperovskites with (i) some other systems such as $NiGa_2S_4$, $Bi_3Mn_4O_{12}(NO_3)$, Gd_2PdSi_3, $GdRu_2Si_2$, and Pd/Fe/Ir (111) for which the competition between magnetic exchange interactions that go beyond nearest-neighbor interaction stabilizes skyrmion lattices [31,47–56] and (ii) with pyrochlore lattice for which a recent work [57] predicted that hedgehog lattice can be induced by frustration. Other topological states were also observed in our MC calculations. An example shown in the Supplemental Material is a skyrmion tube having a diameter of ~ 10Å and propagating in the entire supercell.

In summary, magnetic properties and topological spin textures of antiperovskite ferrimagnet Mn_4N were investigated by *ab-initio* based simulations. The main results are: (1) a sizeable magnetization compensation temperature, T_M, exists within the ferrimagnetic Type-B structure (this T_M may be tuned towards 300K by growing Mn_4N thin films on various substrates, as predicted for epitaxial films made of rare-earth iron garnet systems [19]); (2) nanometric-sized hedgehog-anti-hedgehog pairs were revealed; (3) with these topological states being stabilized by frustrated exchange coupling between 4NN Mn II and Mn III(B) ions. Such predictions thus indicate that frustration can play a critical role to largely reduce the size of topological defects (i.e. to reach nanometric-sized), which is of large benefits to advanced spintronics. We hope our predictions will motivate experimental confirmations of such T_M and hedgehog-anti-hedgehog pairs in antiperovskites and will be put to use to design novel spintronic devices.

Acknowledgment

This work is supported by the Arkansas Research Alliance (T.B. and L.B.) and the Vannevar Bush Faculty Fellowship Grant No. N00014-20-1-2834 (C.X. and L.B.) We also acknowledge the DoD High-Performance Computing Modernization Program (HPCMP) and the Arkansas High-Performance Computing Center (AHPCC) for providing access to the computational clusters.

*cx002@uark.edu

Couplings	J_{xx}	J_{yy}	J_{zz}	E
J_{11}	68.410	68.490	68.380	-136.759
J_{12}	58.500	58.200	59.000	-117.999
J_{13}	18.800	18.800	17.600	17.600
J_{14}	-72.510	-72.510	-73.050	-73.049
J_{21}	-90.100	-90.200	-90.200	-45.100
J_{22}	-50.400	-50.400	-50.400	-25.200
J_{23}	-42.800	-42.600	-43.076	-45.100
J_{24}	-34.000	-34.000	-35.000	-8.750
J_{25}	-1.340	-1.340	-2.300	-0.575
J_{26}	5.800	5.600	5.800	2.900
J_{27}	9.010	8.970	8.480	4.240
J_{31}	-1.800	-1.800	-1.800	-25.200
J_{32}	-0.400	-0.400	-0.400	-0.800
J_{41}	-5.300	-5.300	-5.300	21.200
J_{42}	4.600	4.600	4.600	-18.400

Table 1. Calculated magnetic exchange coupling parameters of Mn_4N up till 4th nearest-neighbor Mn-Mn pairs. E is the energy contribution of each J parameters in the total energy of the ferrimagnetic ground state with respect to the paramagnetic state per unit cell. (unit: meV)

	D_x	D_y	D_z
D_{11}	0.050	-0.185	0.005
D_{12}	0.000	-1.050	0.050
D_{13}	-0.050	-0.050	-3.900
D_{14}	0.050	-0.055	0.000
	A_{xx}	A_{yy}	
Mn I	0.020	0.000	
Mn II	-2.620	-2.640	
Mn III	-0.620	-0.020	

Table 2. Calculated DM interactions of the first nearest-neighbor Mn-Mn pairs and SIA parameters of Mn_4N (unit: meV).

Figure 1. Panel (a) illustrates the schematic of atomic arrangements and Type-B magnetic arrangement in the Mn_4N unit cell. The spins of the Mn III atoms are arranged antiparallel to the spins of the Mn I and Mn II atoms. Panel (b) shows the 2x1x2 supercell of Mn_4N where it displays all the different J parameters that are considered in this study. The frustrated exchange J parameters are colored in black.

Figure 2. Magnetic properties, as predicted from MC simulations. Panel (a) shows the specific heat (arb. units) and panel (b) displays the normalized total magnetic moment, as well as, the individual magnetic moments, as a function of a temperature. Note that the normalization of the individual magnetic moments in Panel b is done to reproduce their DFT values at 0K.

Figure 3. Distribution of topological charge Q and spin textures of two different states possessing hedgehog anti-hedgehog pairs, as found from MC simulations at low temperatures. Panel (a) and (b) show a state with two and four of such pairs, respectively, within the used supercell. The red and blue colors represent opposite signs for Q, and the arrows represent the spin patterns. Note that all the blank spaces within the supercell consists of the ferrimagnetic ground state of Mn_4N.

Figure 4. The relative-decomposed energy contributions of all J parameters for 1NN (a), 2NN (b), 3NN (c), 4NN (d), DMI (e) and SIA (f) for the hedgehog anti-hedgehog pairs shown in Fig. 3a. The relative decomposed energies of J parameters, DMI vectors and SIA that have negative values are shown via stripe patterns.

[1] H. Nakamura, D. Huang, J. Merz, E. Khalaf, P. Ostrovsky, A. Yaresko, D. Samal, and H. Takagi, Nat. Commun. **11**, 1 (2020).

[2] T. He, Q. Huang, A. P. Ramirez, Y. Wang, K. A. Regan, N. Rogado, M. A. Hayward, M. K. Haas, J. S. Slusky, K. Inumara, H. W. Zandbergen, N. P. Ong, and R. J. Cava, Nature **411**, 54 (2001).

[3] R. Yu, H. Weng, Z. Fang, X. Dai, and X. Hu, Phys. Rev. Lett. **115**, 036807 (2015).

[4] Y. Sun, X. Q. Chen, S. Yunoki, D. Li, and Y. Li, Phys. Rev. Lett. **105**, 216406 (2010).

[5] W. F. Goh and W. E. Pickett, Phys. Rev. B **97**, 035202 (2018).

[6] W. J. Takei, R. R. Heikes, and G. Shirane, Phys. Rev. **125**, 1893 (1962).

[7] S. Isogami, K. Masuda, and Y. Miura, Phys. Rev. Mater. **4**, 014406 (2020).

[8] K. Kabara and M. Tsunoda, J. Appl. Phys. **117**, 17B512 (2015).

[9] Y. Yasutomi, K. Ito, T. Sanai, K. Toko, and T. Suemasu, J. Appl. Phys. **115**, 17A935 (2014).

[10] A. Foley, J. Corbett, A. Khan, A. L. Richard, D. C. Ingram, A. R. Smith, L. Zhao, J. C. Gallagher, and F. Yang, J. Magn. Magn. Mater. **439**, 236 (2017).

[11] T. Gushi, M. Jovičević Klug, J. Peña Garcia, S. Ghosh, J.-P. Attané, H. Okuno, O. Fruchart, J. Vogel, T. Suemasu, S. Pizzini, and L. Vila, Nano Lett. **19**, 8716 (2019).

[12] T. Hirose, T. Komori, T. Gushi, A. Anzai, K. Toko, and T. Suemasu, AIP Adv. **10**, 025117 (2020).

[13] X. Shen, A. Chikamatsu, K. Shigematsu, Y. Hirose, T. Fukumura, and T. Hasegawa, Appl. Phys. Lett. **105**, 072410 (2014).

[14] W. Zhou, C. T. Ma, T. Q. Hartnett, P. V. Balachandran, and S. J. Poon, AIP Adv. **11**, 015334 (2021).

[15] K. Ito, Y. Yasutomi, K. Kabara, T. Gushi, S. Higashikozono, K. Toko, M. Tsunoda, and T. Suemasu, AIP Adv. **6**, 056201 (2016).

[16] S. Geprägs, A. Kehlberger, F. Della Coletta, Z. Qiu, E.-J. Guo, T. Schulz, C. Mix, S. Meyer, A. Kamra, M. Althammer, H. Huebl, G. Jakob, Y. Ohnuma, H. Adachi, J. Barker, S. Maekawa, G. E. W. Bauer, E. Saitoh, R. Gross, S. T. B. Goennenwein, and M. Kläui, Nat. Commun. **7**, 10452 (2016).

[17] R. Nakamoto, B. Xu, C. Xu, H. Xu, and L. Bellaiche, Phys. Rev. B **95**, 024434 (2017).

[18] S. Geller, J. P. Remeika, R. C. Sherwood, H. J. Williams, and G. P. Espinosa, Phys. Rev. **137**, A1034 (1965).

[19] T. Bayaraa, C. Xu, D. Campbell, and L. Bellaiche, Phys. Rev. B **100**, 214412 (2019).

[20] R. L. White, J. Appl. Phys. **40**, 1061 (1969).

[21] H. J. Zhao, J. Íñiguez, X. M. Chen, and L. Bellaiche, Phys. Rev. B **93**, 014417 (2016).

[22] L. Caretta, M. Mann, F. Büttner, K. Ueda, B. Pfau, C. M. Günther, P. Hessing, A. Churikova, C. Klose, M. Schneider, D. Engel, C. Marcus, D. Bono, K. Bagschik, S. Eisebitt, and G. S. D. Beach, Nat. Nanotechnol. **13**, 1154 (2018).

[23] S. Woo, K. M. Song, X. Zhang, Y. Zhou, M. Ezawa, X. Liu, S. Finizio, J. Raabe, N. J. Lee, S. Il Kim, S. Y. Park, Y. Kim, J. Y. Kim, D. Lee, O. Lee, J. W. Choi, B. C. Min, H. C. Koo, and J. Chang, Nat. Commun. **9**, 1 (2018).

[24] Y. Quessab, J. W. Xu, C. T. Ma, W. Zhou, G. A. Riley, J. M. Shaw, H. T. Nembach, S. J. Poon, and A. D. Kent, Sci. Rep. **10**, 1 (2020).

[25] C. T. Ma, Y. Xie, H. Sheng, A. W. Ghosh, and S. J. Poon, Sci. Rep. **9**, 1 (2019).

[26] K.-J. Kim, S. K. Kim, Y. Hirata, S.-H. Oh, T. Tono, D.-H. Kim, T. Okuno, W. S. Ham, S. Kim, G. Go, Y. Tserkovnyak, A. Tsukamoto, T. Moriyama, K.-J. Lee, and T. Ono, Nat. Mater. **16**, 1187 (2017).

[27] T. Garel and S. Doniach, Phys. Rev. B **26**, 325 (1982).

[28] N. Nagaosa and Y. Tokura, Nat. Nanotechnol. **8**, 899 (2013).

[29] T. Moriya, Phys. Rev. **120**, 91 (1960).

[30] Y. Xu, G.-L. Yang, D.-P. Chu, and H.-R. Zhai, Phys. Status Solidi **157**, 685 (1990).

[31] T. Okubo, S. Chung, and H. Kawamura, Phys. Rev. Lett. **108**, 017206 (2012).

[32] Y. Miyatake, M. Yamamoto, J. J. Kim, M. Toyonaga, and O. Nagai, J. Phys. C Solid State Phys. **19**, 2539 (1986).

[33] M. R. Hestenes and E. Stiefel, J. Res. Natl. Bur. Stand. (1934). **49**, 409 (1952).

[34] Z. Zhang, Y. Cho, M. Gong, S. T. Ho, J. Singhal, J. Encomendero, X. Li, H. Lee, H. G. Xing, and D. Jena, IEEE Trans. Magn. (2021).

[35] T. Komori, T. Hirose, T. Gushi, K. Toko, T. Hanashima, L. Vila, J.-P. Attanè, K. Amemiya, and T. Suemasu, J. Appl. Phys. **127**, 043903 (2020).

[36] H. Mitarai, T. Komori, T. Hirose, K. Ito, S. Ghosh, S. Honda, K. Toko, L. Vila, J.-P. Attané, K. Amemiya, and T. Suemasu, Phys. Rev. Mater. **4**, 094401 (2020).

[37] T. Tanigaki, K. Shibata, N. Kanazawa, X. Yu, Y. Onose, H. S. Park, D. Shindo, and Y. Tokura, Nano Lett. **15**, 5438 (2015).

[38] Y. Fujishiro, N. Kanazawa, T. Nakajima, X. Z. Yu, K. Ohishi, Y. Kawamura, K. Kakurai, T. Arima, H. Mitamura, A. Miyake, K. Akiba, M. Tokunaga, A. Matsuo, K. Kindo, T. Koretsune, R. Arita, and Y. Tokura, Nat. Commun. **10**, 1059 (2019).

[39] B. Berg and M. Lüscher, Nucl. Physics, Sect. B **190**, 412 (1981).

[40] C. Xu, P. Chen, H. Tan, Y. Yang, H. Xiang, and L. Bellaiche, Phys. Rev. Lett. **125**, 037203 (2020).

[41] J. Seidel, Nat. Mater. **18**, 188 (2019).

[42] K. Everschor-Sitte, J. Masell, R. M. Reeve, and M. Kläui, J. Appl. Phys. **124**, 240901 (2018).

[43] A. K. Nayak, V. Kumar, T. Ma, P. Werner, E. Pippel, R. Sahoo, F. Damay, U. K. Rößler, C. Felser, and S. S. P. Parkin, Nature **548**, 561 (2017).

[44] N. Gao, S. G. Je, M. Y. Im, J. W. Choi, M. Yang, Q. Li, T. Y. Wang, S. Lee, H. S. Han, K. S. Lee, W. Chao, C. Hwang, J. Li, and Z. Q. Qiu, Nat. Commun. **10**, 1 (2019).

[45] B. Göbel, I. Mertig, and O. A. Tretiakov, Phys. Rep. **895**, 1 (2021).

[46] C. Xu, J. Feng, S. Prokhorenko, Y. Nahas, H. Xiang, and L. Bellaiche, Phys. Rev. B **101**, 060404(R) (2020).

[47] B. Dupé, M. Hoffmann, C. Paillard, and S. Heinze, Nat. Commun. **5**, 4030 (2014).

[48] Y. Zhang, C. Xu, P. Chen, Y. Nahas, S. Prokhorenko, and L. Bellaiche, Phys. Rev. B **102**, 241107(R) (2020).

[49] A. O. Leonov and M. Mostovoy, Nat. Commun. **6**, 8275 (2015).

[50] S.-Z. Lin and S. Hayami, Phys. Rev. B **93**, 064430 (2016).

[51] S. Hayami, S.-Z. Lin, and C. D. Batista, Phys. Rev. B **93**, 184413 (2016).

[52] S.-Z. Lin and C. D. Batista, Phys. Rev. Lett. **120**, 077202 (2018).

[53] T. Shimokawa, T. Okubo, and H. Kawamura, Phys. Rev. B **100**, 224404 (2019).

[54] R. Ozawa, S. Hayami, and Y. Motome, Phys. Rev. Lett. **118**, 147205 (2017).

[55] T. Kurumaji, T. Nakajima, M. Hirschberger, A. Kikkawa, Y. Yamasaki, H. Sagayama, H. Nakao, Y. Taguchi, T. Arima, and Y. Tokura, Science (80-.). **365**, 914 (2019).

[56] N. D. Khanh, T. Nakajima, X. Yu, S. Gao, K. Shibata, M. Hirschberger, Y. Yamasaki, H. Sagayama, H. Nakao, L. Peng, K. Nakajima, R. Takagi, T. Arima, Y. Tokura, and S. Seki, Nat. Nanotechnol. **15**, 444 (2020).

[57] K. Aoyama and H. Kawamura, Phys. Rev. B **103**, 014406 (2021).

[58] See Supplemental Material [url] for detailed information on the computational methods, 5th and 6th nearest neighbor interactions, the newly found magnetization compensation temperature, and the topological state called skyrmion tube, which is further found in our Monte-Carlo (MC) simulations, which includes Refs. [32-36,59-66].

[59] G. Kresse and D. Joubert, Phys. Rev. B 59, 1758 (1999).

[60] P. E. Blöchl, Phys. Rev. B 50, 17953 (1994).

[61] J. P. Perdew, K. Burke, and M. Ernzerhof, Phys. Rev. Lett. 77, 3865 (1996).

[62] A. I. Liechtenstein, V. I. Anisimov, and J. Zaanen, Phys. Rev. B 52, R5467 (1995).

[63] K. Ito, Y. Yasutomi, K. Kabara, T. Gushi, S. Higashikozono, K. Toko, M. Tsunoda, and T. Suemasu, AIP Adv. 6, 056201 (2016).

[64] H. Xiang, C. Lee, H.-J. Koo, X. Gong, and M.-H. Whangbo, Dalt. Trans. 42, 823 (2013).

[65] C. Xu, B. Xu, B. Dupé, and L. Bellaiche, Phys. Rev. B 99, 104420 (2019).

[66] M. Mamoru, JPSJ.17.796 17, 796 (2013).

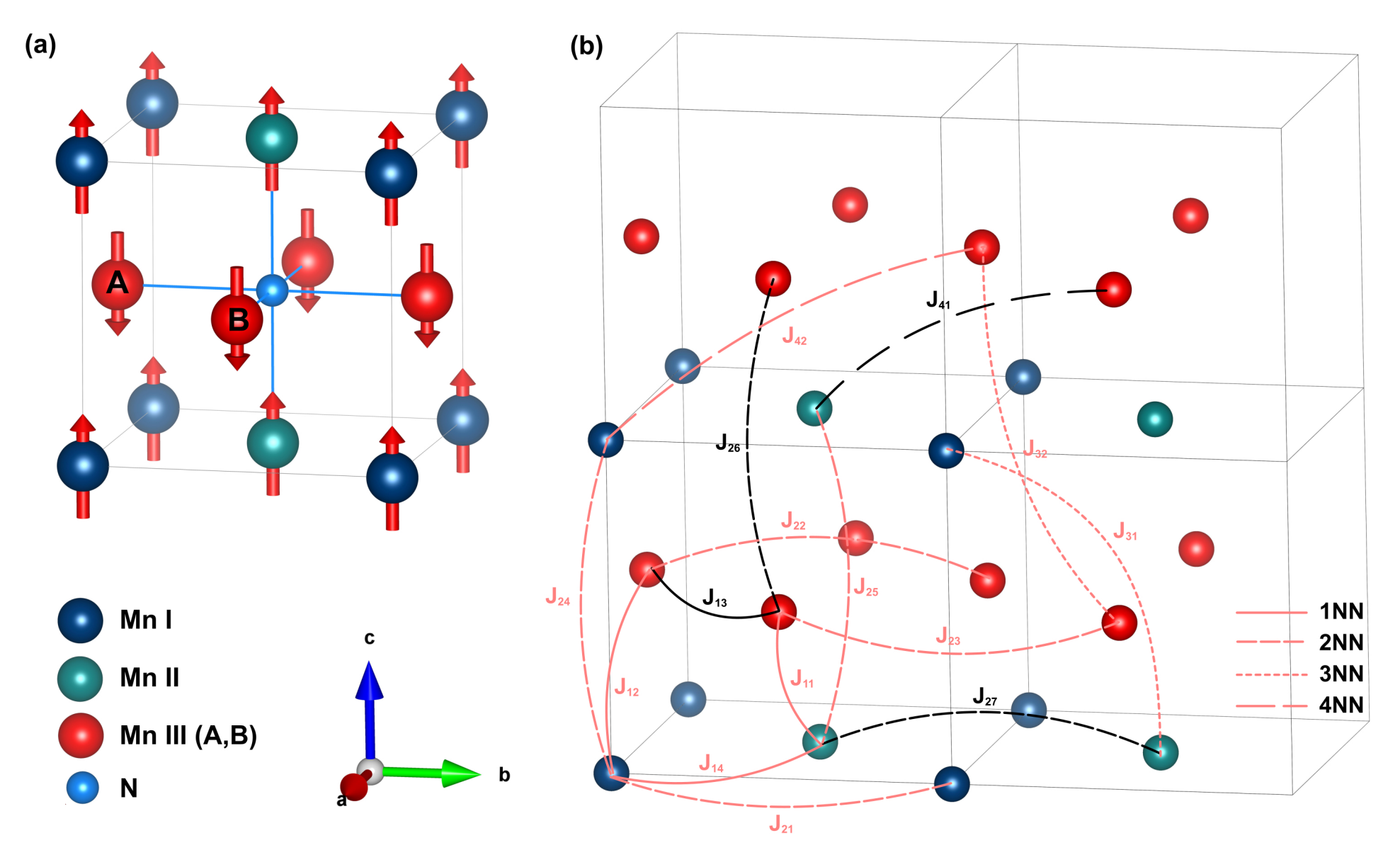
(a)
A
B
Mn I
Mn II
Mn III (A,B)
N
c
b
a
(b)
J41
J42
J26
J32
J22
J31
J24
J13
J25
J23
J12
J11
J27
J14
J21
1NN
2NN
3NN
4NN

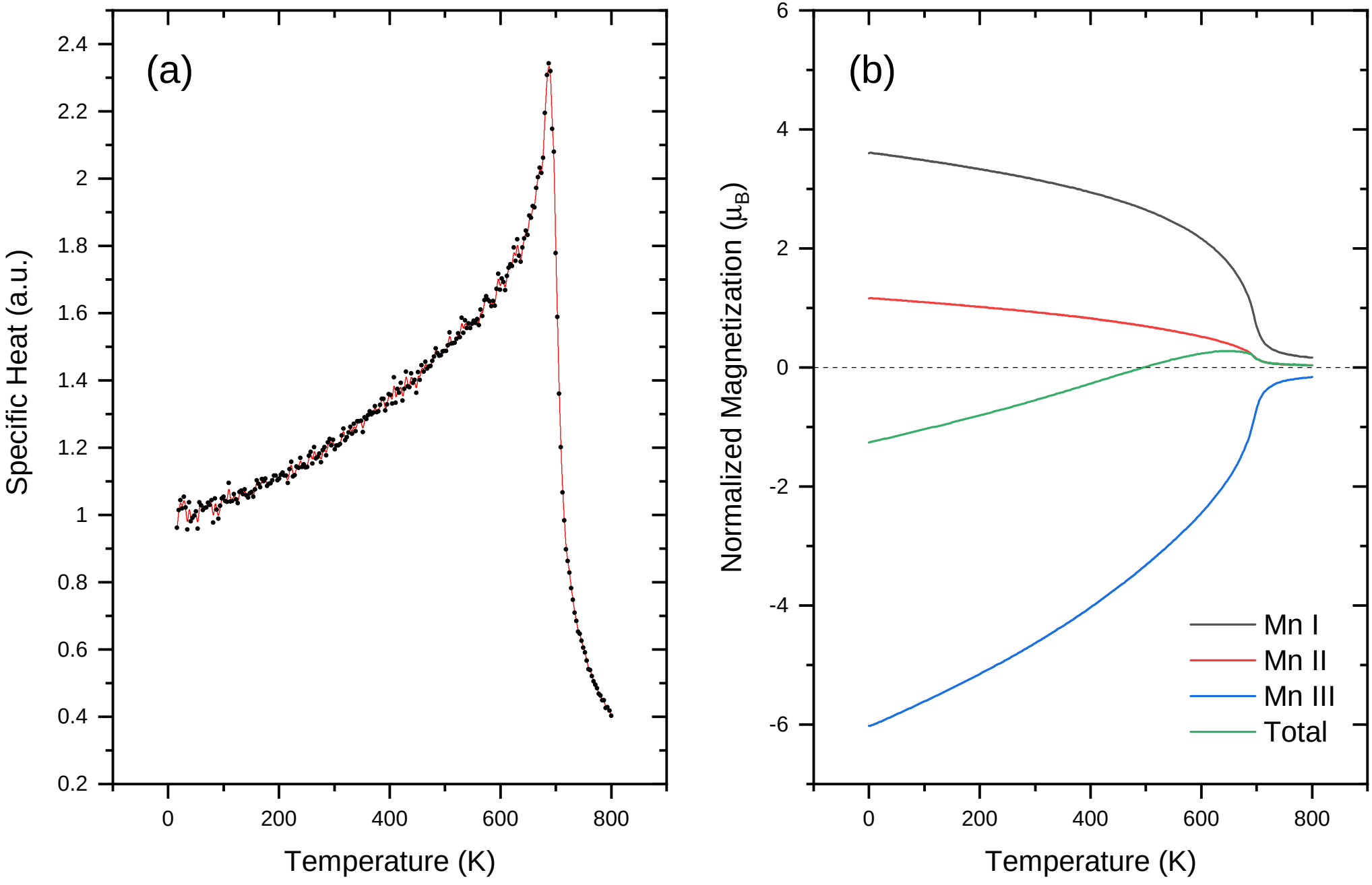
(a)
Specific Heat (a.u.)
Temperature (K)
2.4
2.2
2
1.8
1.6
1.4
1.2
1
0.8
0.6
0.4
0.2
0
200
400
600
800
(b)
Normalized Magnetization (μ_B)
Temperature (K)
6
4
2
0
-2
-4
-6
Mn I
Mn II
Mn III
Total

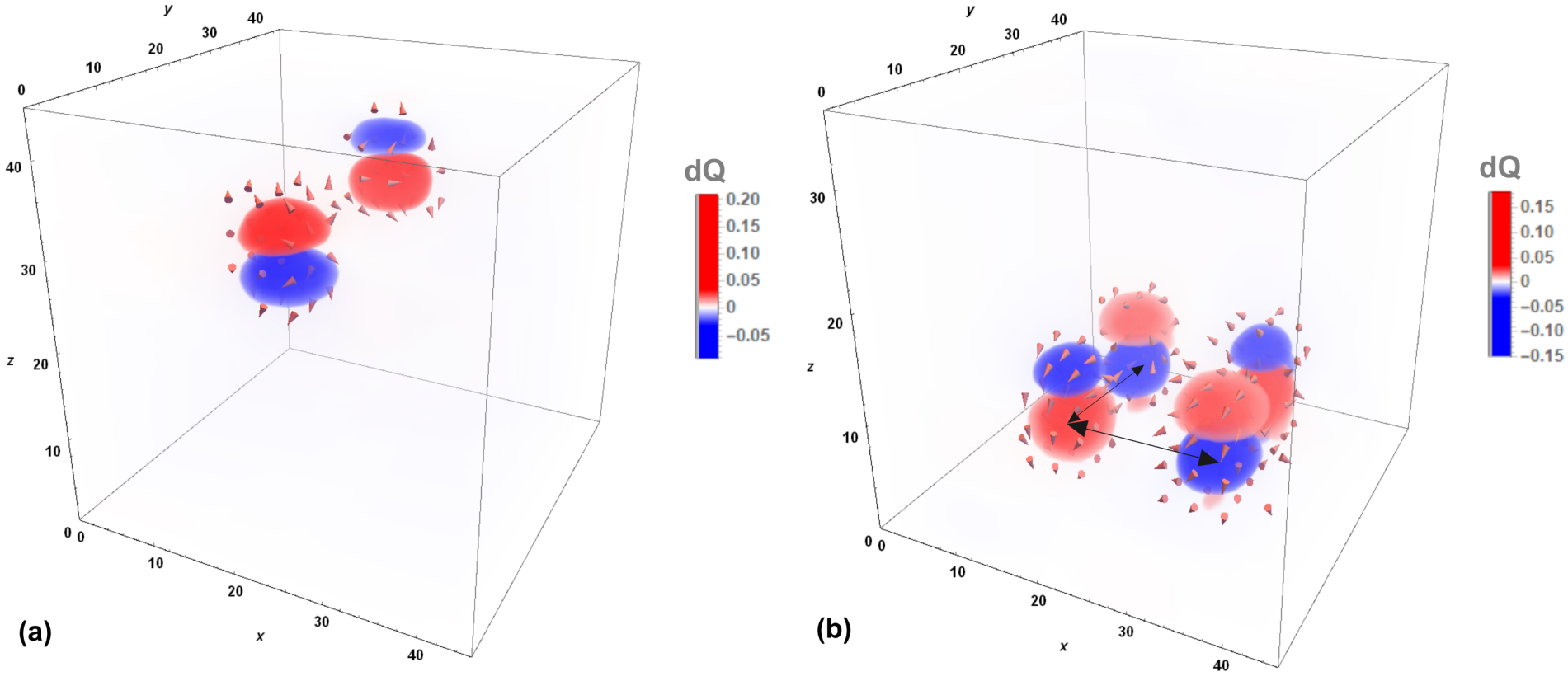
y
0
10
20
30
40
z
0
10
20
30
40
x
0
10
20
30
40
dQ
0.20
0.15
0.10
0.05
0
−0.05
(a)
y
0
10
20
30
40
z
0
10
20
30
x
0
10
20
30
40
dQ
0.15
0.10
0.05
0
−0.05
−0.10
−0.15
(b)

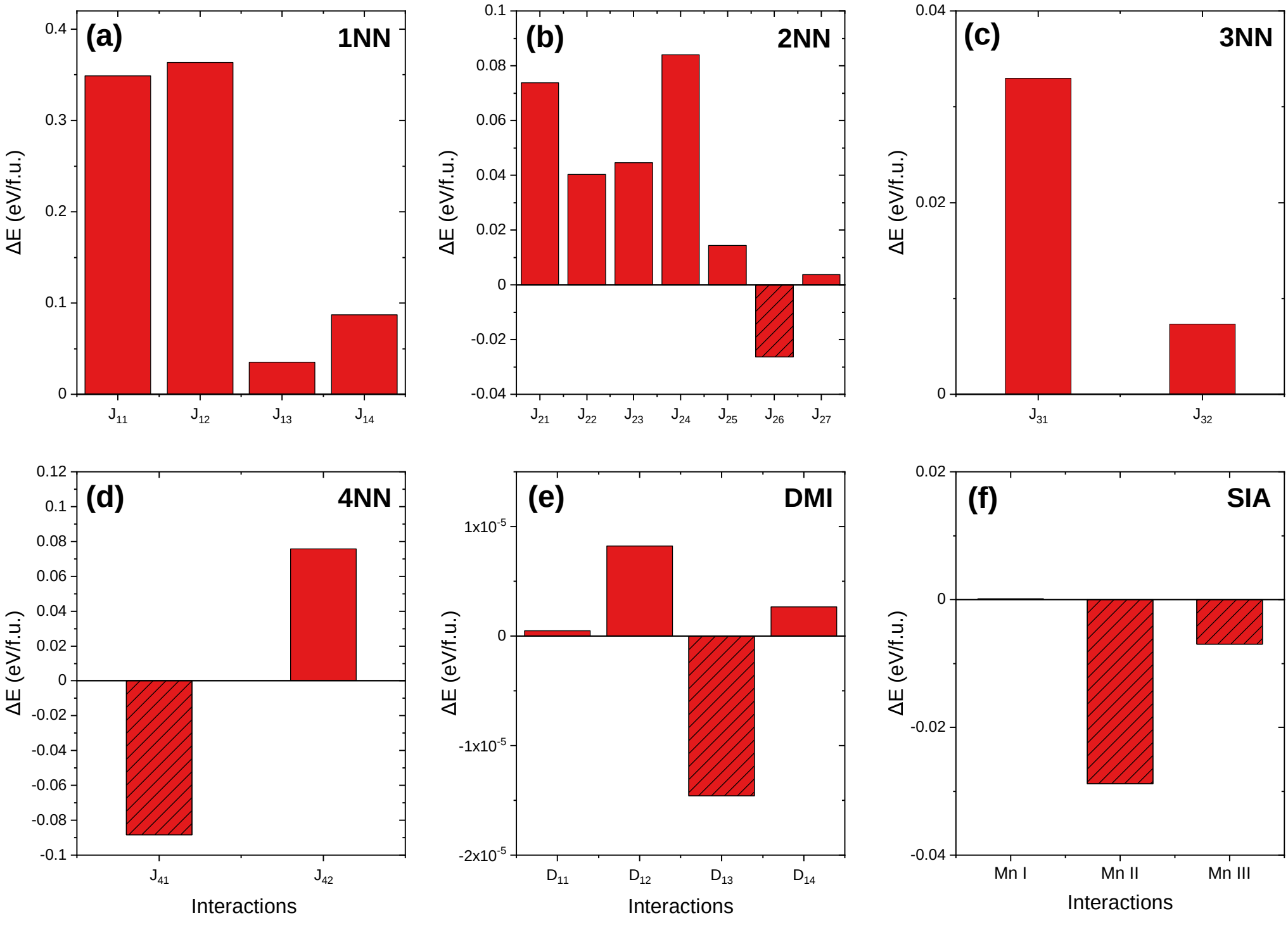
(a)
1NN
ΔE (eV/f.u.)
0.4
0.3
0.2
0.1
0
J11
J12
J13
J14
(b)
2NN
ΔE (eV/f.u.)
0.1
0.08
0.06
0.04
0.02
0
-0.02
-0.04
J21
J22
J23
J24
J25
J26
J27
(c)
3NN
ΔE (eV/f.u.)
0.04
0.02
0
J31
J32
(d)
4NN
ΔE (eV/f.u.)
0.12
0.1
0.08
0.06
0.04
0.02
0
-0.02
-0.04
-0.06
-0.08
-0.1
J41
J42
Interactions
(e)
DMI
ΔE (eV/f.u.)
1x10-5
0
-1x10-5
-2x10-5
D11
D12
D13
D14
Interactions
(f)
SIA
ΔE (eV/f.u.)
0.02
0
-0.02
-0.04
Mn I
Mn II
Mn III
Interactions